

Real-space hole-doping titration and manipulation of correlated charge density wave state in 1T-TaS₂

Haoyu Dong^{1,2,+}, Yanyan Geng^{1,2,+}, Jianfeng Guo^{1,2}, Le Lei^{1,2}, Manyu Wang^{1,2}, Yan Li³, Li Huang³, Fei Pang^{1,2}, Rui Xu^{1,2}, Wei Ji^{1,2}, Hong-Jun Gao³, Weichang Zhou^{4,*}, and Zhihai Cheng^{1,2,*}

¹Key Laboratory of Quantum State Construction and Manipulation (Ministry of Education), Renmin University of China, Beijing, 100872, People's Republic of China

²Beijing Key Laboratory of Optoelectronic Functional Materials & Micro-nano Devices, Department of Physics, Renmin University of China, Beijing 100872, People's Republic of China

³Beijing National Laboratory for Condensed Matter Physics, Institute of Physics, Chinese Academy of Sciences, Beijing 100190, People's Republic of China

⁴Key Laboratory of Low-dimensional Quantum Structures and Quantum Control of Ministry of Education, School of Physics and Electronics, Institute of Interdisciplinary Studies, Hunan Normal University, Changsha 410081, People's Republic of China

Abstract: The complex correlated charge density wave (CDW) phases of 1T-TaS₂ have attracted great attention due to their emergent quantum states, such as intricate CDW phase, Mott-Hubbard state, superconductivity and quantum spin liquid. The delicate interplay among the complex intra-/inter-layer electron-electron and electron-lattice interactions is the fundamental prerequisite of these exotic quantum states. Here, we report a real-space titration-like investigation of correlated CDW state in 1T-TaS₂ upon hole-doping via low-temperature scanning tunneling microscopy (LT-STM). The gradual increased hole-doping results in the sequential emergence of electron voids, phase domains, stacking disordering and mixed phase/chiral domains attributed to the reduced electron correlations. The achiral intermediate ring-like clusters and nematic CDW states emerge at the intralayer chiral domain wall and interlayer heterochiral stacking regions via the chiral-overlapping configurations. The local reversible CDW manipulation is further realized by the non-equilibrium transient charge-injections of STM field-emission spectra. Our results provide an in-depth insight of this intricate correlated CDW state, and pave a way to realize exotic quantum states via the accurate tuning of interior interactions in correlated materials.

⁺These authors contributed equally: Haoyu Dong, Yanyan Geng

*Email: zhihaicheng@ruc.edu.cn, wchangzhou@hunnu.edu.cn

Introduction

Charge density wave (CDW) materials host correlated electronic states typified by periodic atomic lattice distortions and delicate tuning of correlated electrons [1-2]. Recently, the van der Waals (vdW) layered transition metal dichalcogenides (TMDs) materials have attracted significant attention due to the emergent exotic quantum states resulting from their competition and/or cooperation with the preemergent intricate CDW states [3-5]. Among the diverse TMD materials, $1T$ -TaS₂ has evoked great research interest as a prototypical CDW material platform for investigating the CDW order and strong electron correlations [6-10]. From the high-temperature normal metallic phase, $1T$ -TaS₂ undergoes a sequential CDW phase of incommensurate CDW (ICCDW), near commensurate CDW (NCCDW) and commensurate CDW (CCDW), as shown in Supplementary Fig. 1, during the cool-down process [10-12]. In the ground CCDW state, the Star of David (SoD) CDW distortion with a perfect $\sqrt{13}\times\sqrt{13}$ triangular superlattice is observed in $1T$ -TaS₂ with the intralayer Mott-Hubbard electronic characteristics of unpaired spin-1/2 electrons. Recently, it has become the focus of attention on the interior electron-electron correlations and electron-lattice interactions for a deep insight of the emergent Wigner crystal [13-14], quantum spin liquid [15-18] and topological superconductor [19-20] in pristine $1T$ -TaS₂ and its related materials.

In addition to their intrinsic states, many exotic and novel phenomena or states, such as mosaic CDW state [21-24], hidden state [25-28], quantum jamming [29], superconductivity [30], Kondo lattice [31] and Kagome structure [32-33], have been realized through the various global and local perturbations of $1T$ -TaS₂, including electrostatic gating [34], laser [33,35-36] and voltage pulses [21-23], surface atomic adsorption [37-39], precise temperature control [12,32,40], heterogeneous stacking [41], and so on. Only very recently, the intrinsic chirality of correlated CDW state has become the hot research topic of $1T$ -TaS₂, including the emergence of chiral domains [42-43], switching of interlayer heterochirality [44] and electrical switching of intralayer ferro-rotational order [45]. Precise charge-doping is also a feasible method of effectively control correlated electronic materials, which can gradually regulate the interior electron-electron correlations to induce exotic quantum states without noticeable structural changes [8,42]. In the CDW-based chiral Mott-Hubbard electronic

system, charge-doping not only can directly affect the interior electron-electron correlations but also may induce significant CDW structural changes with the consequential intricate electron-lattice interactions. Therefore, a detailed study of the doping-dependent structure and properties of $1T\text{-TaS}_2$ is the necessary prerequisite for the controllable emergence of exotic quantum states from the CDW-based chiral correlated states.

In this work, we report a real-space investigation of correlated interactions in the CDW state of $1T\text{-TaS}_2$ by titration-like hole-doping via LT-STM. With the increased hole-doping and weakened electron-electron correlations, the sequential emergence of electron voids, phase domains, stacking disorder, and mixed phase/chiral domains is observed. At the primary stage, the emergence of fragmentized intralayer phase domains and metastable interlayer stacking can be attributed to the reduced electron correlations, which is incapable of persisting long-range intralayer and interlayer order. The further decreased electron correlations and electron-lattice interactions contributed to the following emergence of intralayer chiral domains and interlayer heterochiral stacking. At the intralayer chiral domain wall and interlayer heterochiral stacking regions, the intermediate ring-SoD clusters and nematic CDW states are discovered and discussed based on the transient chiral-overlapping interactions. Additionally, the local reversible ordering-disordering manipulation of CDW state was realized by the transient non-equilibrium charge-injection of STM field-emission bias-pulse. This work shed considerable light on the insight of interior interactions and the future realization of exotic quantum states in correlated electron materials.

Results and discussion

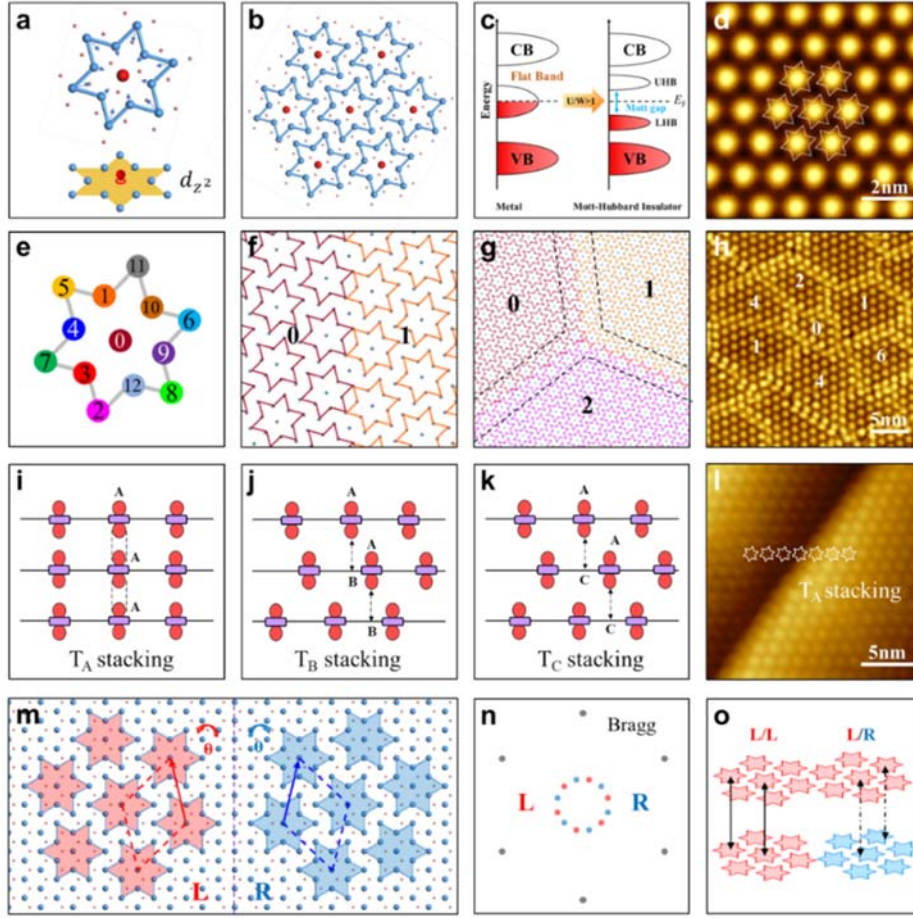


Figure 1. Atomic and electronic structure of the correlated CDW state in 1T-TaS₂. (a) Atomic models of the SoD cluster with the localized d_{z^2} orbital (unpaired electron) of central Ta atom. (b) Schematic illustration of the SoD clusters with the $\sqrt{13} \times \sqrt{13}$ periodicity. (c) Schematic band structures of correlated CDW state, in which the half-filled flat band of the localized d_{z^2} orbital is split into UHB and LHB bands via electron correlations. (d) STM image of commensurate CDW state with the overlaid SoD models. (e,f) Atomic Ta-indexed model (e) of the SoD cluster for the definition of CDW phase domain wall (DW, f). A DW is defined as the center of SoD cluster of the neighboring domain sits on Ta atomic sites of 1-12, as shown by the example of DW-1 in (f). (g) Schematic illustration of a vortex consisting of three DWs. (h) Typical STM image of mosaic CDW state induced by STM bias-pulse. (i-k) Schematic illustrations for the T_A (i), T_B (j), and T_C (k) stacking marked with the central half-filled orbital of SoDs. The interlayer T_A, T_B and T_C stacking were defined by the out-of-plane alignment of Ta-0, Ta-1,3,4,9,10,12 and Ta-2,5,6,7,8,11 defined in (e), respectively. (l) STM image of a step edge showing the common T_A stacking. (m) Schematic of the L- and R- chiral CDW phases marked by red and blue stars, respectively. The mirror-symmetric L- and R-SoD superlattices were marked by dashed lines. (n) Schematic FFT pattern of L- and R-chiral CDW domains with the atomic Bragg spots. (o) Schematic of the homochiral and heterochiral interlayer stackings. Scanning parameter: (d) $V=0.4\text{V}$, $I=100\text{pA}$; (h,l) $V=0.6\text{V}$, $I=100\text{pA}$.

Correlated CDW state

The ground CDW state of 1T-TaS₂ consists of the commensurate $\sqrt{13}\times\sqrt{13}$ superlattice of SoD clusters, as shown in Fig. **1a-b**. The SoD cluster is made of 12 inward-distorted outer Ta atoms and one center Ta atom, in which the twelve $5d_{z^2}$ electrons of the outer Ta atoms pair and form six occupied CDW valence bands. The remaining one unpaired electron of SoD is maximally localized at the central Ta atom to form the half-filled flat band, which is further split into the upper Hubbard band (UHB) and lower Hubbard band (LHB) bands due to the strong intralayer electron-electron correlations (Fig. **1c**). Fig. **1d** shows the STM image of the correlated CDW state with the overlaid star models of SoDs.

Phase domains and domain walls

The superlattice structure of correlated CDW in 1T-TaS₂ with the underlying atomic lattice can lead to the formation of 13 phase domains separated by 12 different domain walls (DWs), as shown in Fig. **1e-h**. The different phase domains and DWs can be defined by the relative positions of the central Ta atoms in the neighboring phase domains. The SoDs of 12 phase DWs show various overlapping structural configurations and stabilities (Supplementary Fig. 2) [23]. The crossing of three straight phase DWs can further form the CDW vortex structures (Fig. **1g**). In contrast to the stable ground CCDW state, the above metastable states can be introduced by STM bias-pulse, and laser pulse to form the mosaic state (local metastable hidden state) [23-27]. Fig. **1h** shows the STM image of the bias-pulse-induced mosaic state, which consist of various phase CDW domains, DWs and CDW vortexes.

Interlayer stacking configurations

The superlattice structure of correlated CDW with the underlying atomic lattice can also lead to the more complex interlayer stacking configurations. The three typical stacking of T_A, T_B and T_C are defined by the out-of-plane alignment of central Ta atoms in the neighboring layers and schematically shown in Fig. **1i-k**. Figure **1l** shows the STM image of the most common and stable T_A stacking configurations confirmed by the overlaid SoD models across the step edges. It is noted that, in the T_A stacking configuration, the central local half-filled d_{z^2} orbitals of interfacial neighboring SoDs can hybridize into the trivial spin-paired dimerized band insulating state in competition with the intralayer Mott-Hubbard insulating state [46-51]. The interlayer hybridization was proven to decrease during the thermal

fluctuations at elevated temperatures [23].

Chiral CDW domains

The $\sqrt{13}\times\sqrt{13}$ superlattice structure of SoDs with the underlying atomic lattice can also lead to the two kinds of mirror-symmetric chiral CDW domains, as shown in Fig. **1m-o**. In the L- and R-chiral CDW domains, the SoD superlattices are rotated clockwise by -13.9° and $+13.9^\circ$ from the atomic lattice of Ta, respectively. In general, the lateral size of the $\sqrt{13}\times\sqrt{13}$ domain of a SoD superlattice in $1T$ -TaS₂ is much larger than normal scan range of STM measurements of about a few hundred nanometers [7], and their interlayer stackings are almost exclusively preferred to the homochiral stacking even in different phase stacking configurations. Only very few works about the chiral CDW state were just reported recently with the focus on their global chiral-switching via the circularly polarized light or electrical pulse in the nanothick flakes [40,52]. The heterochiral CDW DWs and stacking configurations are shown in Supplementary Fig. 3 and rarely investigated. The heterochiral overlapping (intralayer) or stacking (interlayer) of CDW domains could form a super-superlattice of 13×13 ($\sqrt{13}\times\sqrt{13}$) with respect to the underlying atomic (SoD) lattice.

Hole-doping structural titrations

In the pristine $1T$ -TaS₂, the formation of the long-ranged commensurate CDW state is from the interplay/competition of intralayer and interlayer interactions, including the electron-electron correlations and electron-lattice couplings. The enhanced thermal fluctuations at elevated temperatures can adjust the delicate interplay of these complexed interactions to form a series of CDW phases. The charge-doping effects in $1T$ -TaS₂ have been discussed in different ways, including the emergent superconductivity of copper-intercalated bulks and gate-tunable nanothick flakes, which may also affect atomic structure (Supplementary Fig. 4) [43,45]. It is very promising and important to further investigate the electron-filling-dependent CDW states with the focus on their complicated CDW intralayer and interlayer configurations and interactions in a titration-like way, as shown in Supplementary Fig. 5. The electron-filling of flat band in correlated CDW state can be gradually reduced by controllable hole-doping in the Ti-doped $1T$ -Ta_{1-x}Ti_xS₂ (Supplementary Fig. 6) [42], which is investigated in our following work.

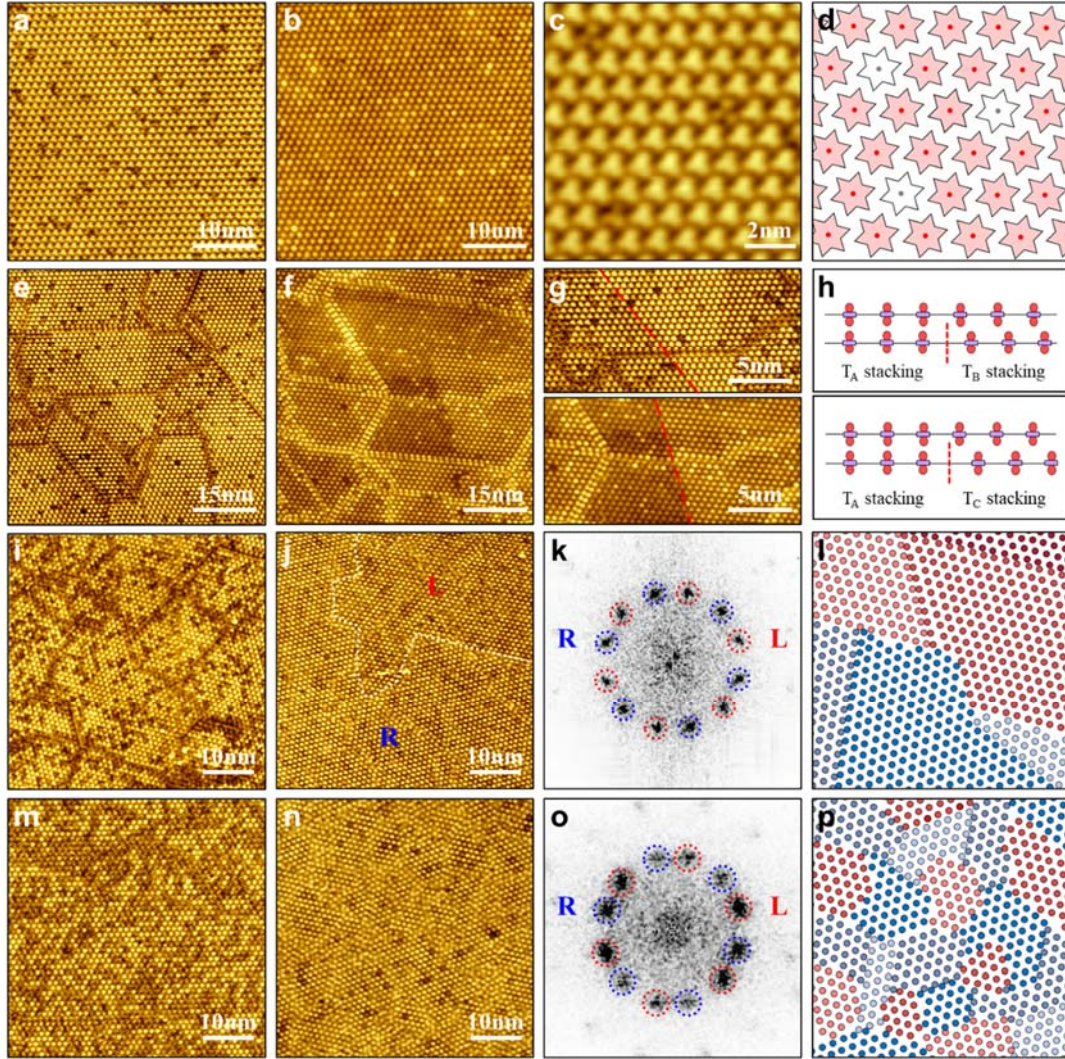


Figure 2. STM measurements of sequential structural titration in hole-doped $1T\text{-TaS}_2$. (a-d) Large-scale occupied state (a), unoccupied state (b) and high-resolution (c) STM images of tiny-hole-doped $1T\text{-TaS}_2$, and their schematic model (d). The central electron-filled and -void SoDs are marked by the central red and grey dots, respectively. (e-h) Large-scale occupied state (e), unoccupied state (f) and high-resolution (g) STM images of mosaic-like low-hole-doped $1T\text{-TaS}_2$, and the possible stacking models (h). The step-like features of surface layer are due to the different stacking order via the phase domains of the underlying layers, as schematically shown by the dashed lines in (g,h). (i-l) Large-scale occupied state (i), unoccupied state (j) STM images and their typical FFT pattern (k) of medium-hole-doped $1T\text{-TaS}_2$, and their structural model (l). The emergent large chiral CDW domain is made of many small homochiral phase domains. The L- and R-chiral domains are separated by white dotted lines in (j), and schematically illustrated in (l). (m-p) Large-scale occupied state (m), unoccupied state (n) STM images and their typical FFT pattern (o) of high-hole-doped $1T\text{-TaS}_2$, and their structural model (p). The fragmented CDW state is made of randomly distributed tiny phase and chiral domains, schematically illustrated in (p). Scanning parameter: (a,c,e,i,m) $V=-0.4\text{V}$, $I=-100\text{pA}$; (b,f,j,n) $V=0.4\text{V}$, $I=100\text{pA}$.

Distributed void SoDs

At the tiny-hole-doping level, as shown in the STM images of Fig. 2a and b, the discretely distribution electron void SoDs emergent within the commensurate SoD superlattice, showing darker (brighter) contrast than the normal SoDs at the occupied (unoccupied) state. These void SoDs without the central localized electrons are clearly resolved as the darker clover shapes in the high-resolution STM image of Fig. 2c, and further schematically illustrated in Fig. 2d. The discretely distribution of individual void SoDs is also consistent with the repulsive electron-electron correlations of partial-filled flat-band in the correlated CDW state. The atomic-resolved AFM measurements have been performed to confirm the electron-void nature of these emergent clover-shaped SoDs at the tiny-hole-doping level.

Phase domains & stacking configurations

At the low-hole-doping level, as shown in the STM images of Fig. 2e and f, the mosaic-like CDW states are observed with the emergent phase domains and DWs, which is in general similar with the pulse-induced metastable mosaic CDW state in pristine 1T-TaS₂. It is noted the mosaic-like CDW states are the stable ground state in the thermal equilibrium, which is existent in each layer due to the hole-doping and different from the metastable (by the external energy excitations) mosaic state of surface layers. The decreased intralayer electron-electron correlations is not enough to sustain the long-range phase ordering of correlated CDW state at the low-hole-doping level. In addition, the consequent various local interlayer stacking configurations further contribute the complexity of these mosaic-like CDW states, such as the marked step-like intra-domain features (Fig. 2g), which should be due to the DWs on the underlying bottom layer (Fig. 2h). The stacking-sensitive interlayer hybridizations led to the different apparent contrasts in the surface-sensitive STM images.

Chiral CDW domains

At the medium-hole-doping level, as shown in the STM images of Fig. 2i and 2j, the mosaic-like CDW states can still be observed, while no apparent stacking-sensitive contrast is resolved in the STM measurements due to the further reduction of interlayer electronic hybridizations. In addition, the large chiral CDW domains emergent within the mosaic-like CDW states, as shown by the marked chiral DWs to separate the R- and L- chiral domains in

Fig. 2j and the corresponding FFT pattern of Fig. 2k. The large chiral domains are made of many small homochiral phase domains, as schematically illustrated in Fig. 2l. It is also noted that, different from the DWs at low-doping-level, the DWs of Fig. 2i and 2j could not be readily resolved based on their specific local contrast. These results indicate that the further decreased electron-electron correlations are not enough to sustain the chiral ordering of correlated state at the medium-hole-doping level.

Mixed phase and chiral domains

At the high-hole-doping level, as shown in the STM images of Fig. 2m and 2n, the fragmented CDW states are observed, which is made of randomly distributed tiny phase and chiral domains. The short phase and chiral DWs are disordered and could not be clearly defined, consistent with the faint electron-electron correlations. The FFT pattern of Fig. 2o is generally similar to that of Fig. 2k but with more blurred and diffused FFT spots, representing the heavily disrupted CDW phase and chiral domains illustrated in Fig. 2p. More images of sequential structural titration in hole-doped 1T-TaS₂ were shown in Supplementary Fig. 7.

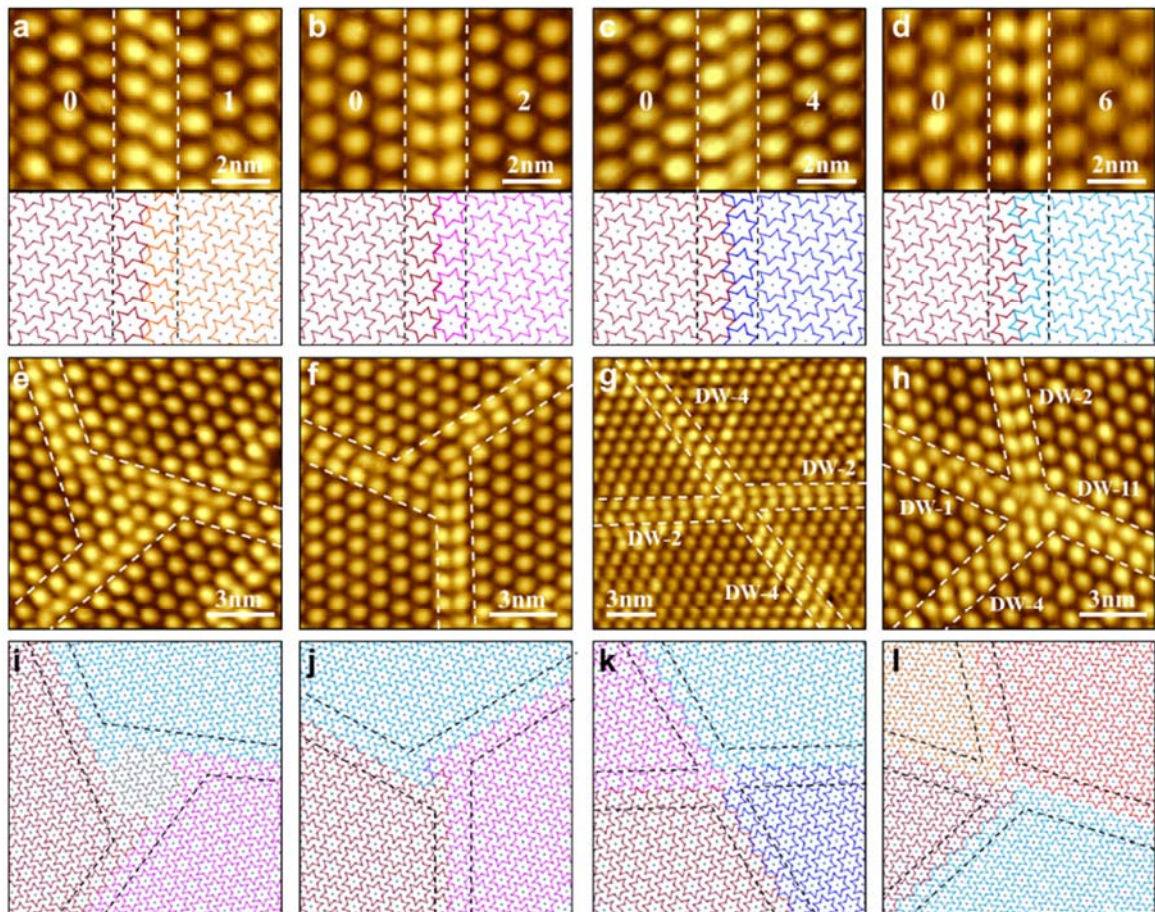


Figure 3. Intralayer CDW phase domain walls and vortex of low-hole-doped 1T-TaS₂. (a-d) STM images of four typical CDW phase DWs (top) and their schematic structural configurations (bottom). The constituent SoDs of phase DWs are highlighted by the dashed lines separating the two neighboring phase domains. The overlapping between the SoDs of DWs in (a-d) gradually increases, leading to reduced structural stability as a result of stronger inter-SoD repulsive interactions. (e-l) STM images of four typical CDW vortexes and their schematic structural configurations (i-l). The constituent SoDs of phase DWs and CDW vortexes are highlighted by the dotted lines separating the three/four CDW phase domains. Scanning parameter: $V=0.4\text{V}$, $I=100\text{pA}$.

Phase domain walls and vortex

Figure 3a-d show the STM images of four emergent phase DWs in the low-hole-doped 1T-TaS₂, in which the DWs of 3a and 3b are frequently observed. While the DWs of 3c and 3d could only be occasionally and rarely observed in STM experiments. It is noted that the SoDs of DWs in 3a-d shows gradual increased overlaps, consistent with their gradual reduced proportions. It can be concluded that the overlap-dependent inter-SoD repulsive electron correlations determine the different structural stabilities of DWs, the larger overlap, the less structural stability. These observed DWs in the thermal stable mosaic-like CDW state of low-hole-doped 1T-TaS₂ is generally consistent with those in the pulse-induced metastable mosaic state of pristine 1T-TaS₂, while the latter can be recovered into the ordered CCDW state at elevated temperatures (Supplementary Fig. 8) [23]. Fig. 3e-h show the STM images of four emergent CDW vortexes in the low-hole-doped 1T-TaS₂, in which the two three-fold symmetric chiral CDW vortexes of 3e,3f are made of three stable DWs of 3a,3b respectively. Fig. 3g shows the intersection of DW-2 and DW-4 with the symmetric shifting in both DWs, resulting in the formation of a chiral 4-vortex. More irregular CDW vortexes were also observed in the mosaic-like CDW state, such as the 4-vortex of Fig. 3h, which is the cross intersection of four different DWs.

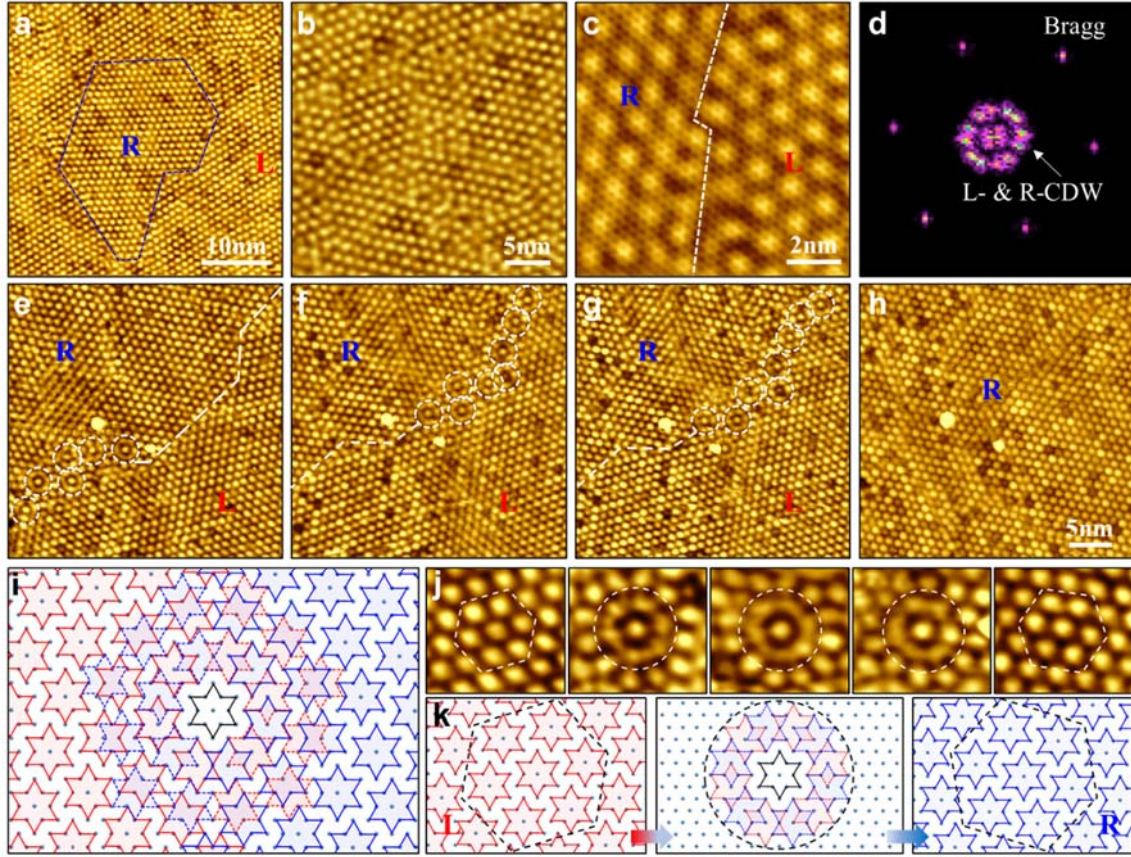


Figure 4. Intralayer CDW chiral domains and chiral-switching transition of hole-doped 1T-TaS₂. (a,b) STM images of large chiral domains (a) and mixed small chiral/phase domains (b). The chiral DW is along the [110] directions of R-chiral domain and marked by blue dashed lines in (a). (c,d) Atomic-resolution STM image (c) of typical chiral DWs and its corresponding FFT pattern (d) with marked Bragg and chiral CDW spots. The chiral DW is marked by white dashed lines. (e-h) A sequential *in-situ* STM images showing the emergent intermediate ring-SoD clusters and their dynamic chiral-switching at the chiral DWs. The ring-SoD clusters are marked with the dashed circles. (i) Chiral SoD-overlapping model of the mirror-symmetric DW with the central achiral SoD. (j,k) A series of selected STM images (j) showing the dynamic chiral-switching transition via the transient intermediate ring-SoD cluster and the proposed structural models (k). Scanning parameter: $V = 0.4\text{V}$, $I = 100\text{pA}$.

Chiral domains walls

In the large chiral CDW domain state, a predominant chirality such as L- chirality in Fig. 4a can be identified with a stable chiral DW along the [110] directions of R-chiral CDW domain (Supplementary Fig. 9). While in the mixed chiral/phase domains state of Fig. 4b, even the chiral DWs can clearly defined with the coexistent imperfect SoDs at the short metastable DWs. The atomic-/SoD-resolution characterizations of these fragmented DWs were further performed, as depicted in Fig. 4c, indicating the perfect continues atomic lattice across the DWs without any visible doping-induced atomic defects and/or dislocations.

Additionally, the corresponding FFT image in Fig. 4d clearly exhibits the sharp atomic lattice spots and the L- /R-chiral CDW lattice spots. It indicated that the SoD superlattice of small CDW domains persists near the DWs even without long-range order, demonstrating the dominant roles of local electron-lattice and short-range inter-SoD interactions in the formation of SoD superlattice.

Intermediate ring-SoD clusters

The delicate interactions can be further titrated by raising the sample temperature (~50K) to investigate the dynamic change of metastable mirror-symmetric chiral DWs by the sequential *in-situ* STM characterizations (identified by the bright spots), as depicted in Fig. 4e-h. A series of novel ring-shaped structures emerged and marked by dashed white circles, which specifically aggregated at the chiral DWs and named as ring-SoD cluster. As the thermal-excited dynamic structures, these ring-SoD clusters could “move” along the chiral DWs and/or as the dynamic intermediate electronic states of SoDs during the chiral-switching transitions (Supplementary Fig. 10). These emergent ring-SoD clusters consist of a central SoD surrounded with a non-chirality ring structure. Figure 4i shows the proposed atomic structure model of these intermediate ring-SoD clusters with the overlapping of R-/L-chiral SoDs, which features a unique central achiral SoD as the anchor points to stabilize the dynamic chiral-switching SoDs. Fig. 4j shows a series of selected STM images to demonstrate the evolution process of chiral-switching transition via the intermediate ring-SoD clusters, schematically illustrated by the atomic models of Fig. 4k (Supplementary Fig. 11). The emergence of ring-SoD clusters as the transient intermediates further indicates the dominant neighboring interaction between the SoDs via the local electron-electron and electron-lattice correlations.

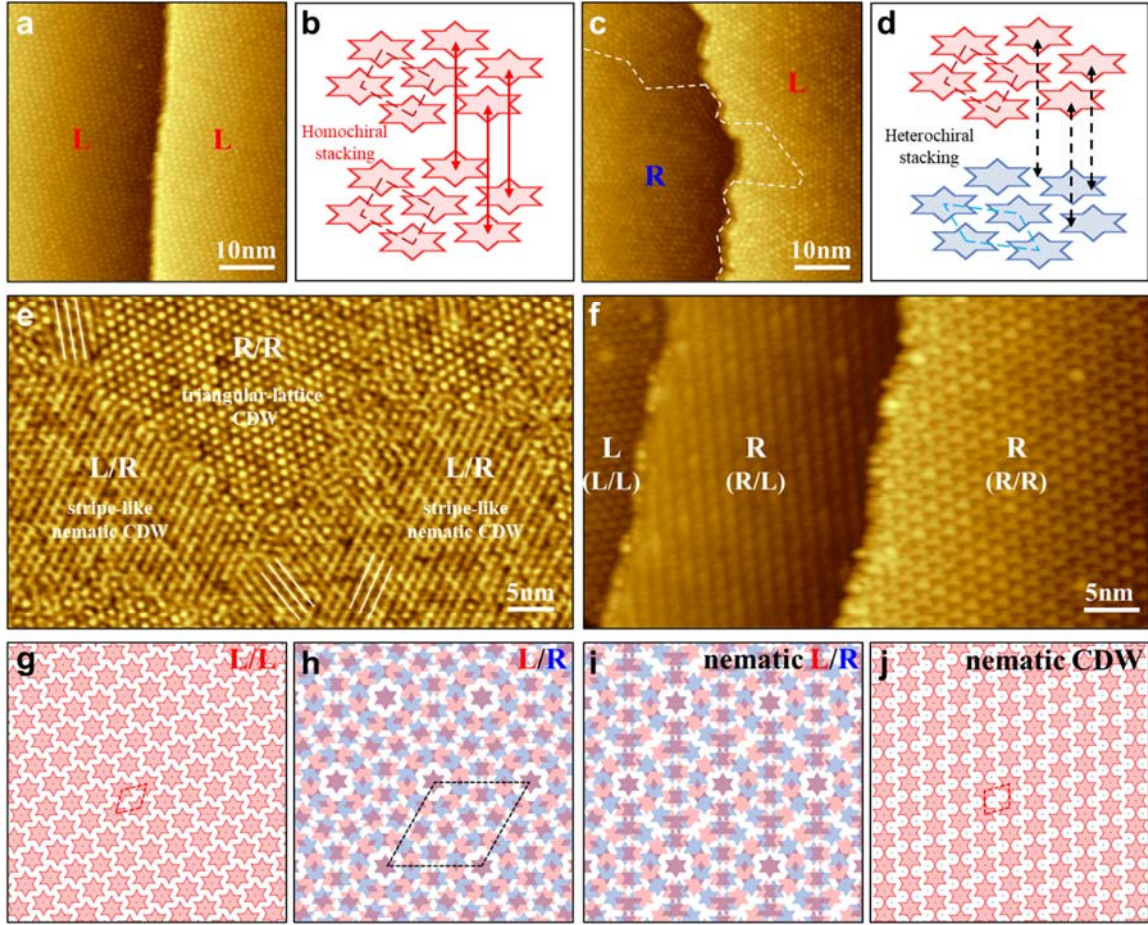


Figure 5. Interlayer CDW chiral stacking and the emergent nematic CDW state of hole-doped 1T-TaS₂. (a,b) STM images of step edge showing the homochiral stacking (a) and its schematic models (b). (c,d) STM images of step edge showing the coexistent homochiral/heterochiral stacking (c) and the schematic model of heterochiral stacking (d). (e) STM image of the chiral domain states with the emergent stripe-like nematic CDW state due to heterochiral stacking configuration. (f) STM image of two step edges with respective homochiral/heterochiral stacking configurations and the accompanying stripe-like feature of nematic CDW state. (g,h) Schematic illustrations of homochiral (g) and heterochiral (h) stacking superstructures. (i) Proposed directional relaxed heterochiral stacking configurations for the observed stripe-like pattern of nematic L/R stacking. (j) Structural model of the stripe-like nematic CDW state. Scanning parameters: (a,c,f) $V=-0.4\text{V}$, $I=-100\text{pA}$; (e) $V=0.4\text{V}$, $I=100\text{pA}$.

Homo- and hetero-chiral stacking

The hole-doping effect on the interlayer interaction can be analyzed via the detailed investigation of the chiral stacking configurations. At tiny-hole-doping levels in Fig. 5a, there are no distinct chiral domains observed in both the upper and lower layers, shows a behavior of homochiral stacking (Fig. 5b), which is consistent with pristine 1T-TaS₂. Two distinct chiral domains emerge simultaneously within both the upper and lower layers in medium-hole-doping level in Fig. 5c, while the chirality between the upper and lower layers

becomes irrelevant, causing a possibility of heterochiral stacking as shown in Fig. 5d. It is clear that the reduced electron-filling of flat band weakens the interlayer electron-electron correlations of SoDs, which fails to maintain the consistent interlayer chirality.

Nematic CDW state

A novel stripe-like feature was observed immediately after the emergence of the intermediate ring-SoD clusters at elevated temperatures (Fig. 5e and Supplementary Fig. 12). All these stripe-like features are along the [211] directions of the underlying atomic lattice, and defined as the nematic CDW state with respect to the underlying atom/SoD triangular lattice. The emergence of nematic CDW state is induced by interlayer heterochiral stacking configuration, which is directly demonstrated by the observed CDW states around the homochiral and heterochiral stacking edges in Fig. 5f. Figure 5g-j schematically illustrate the proposed formation mechanism of this nematic CDW state. Different from the homochiral stacking configuration L/L (Fig. 5g), the heterochiral stacking configuration L/R (Fig. 5h) shows a larger and unstable super-superlattice of 13×13 ($\sqrt{13} \times \sqrt{13}$) with respect to the underlying atomic (SoD) lattice. Then, this huge super-superlattice undergo sequential structural relaxation to an intermediate nematic L/R structure (Fig. 5i) and the final nematic CDW state (Fig. 5j). As a unique chiral-related nematic CDW state, both the formation mechanism and the intriguing atomic/electronic structures are worthy of further deepen theoretical investigations via the intra- and inter-layer inter-SoD interactions.

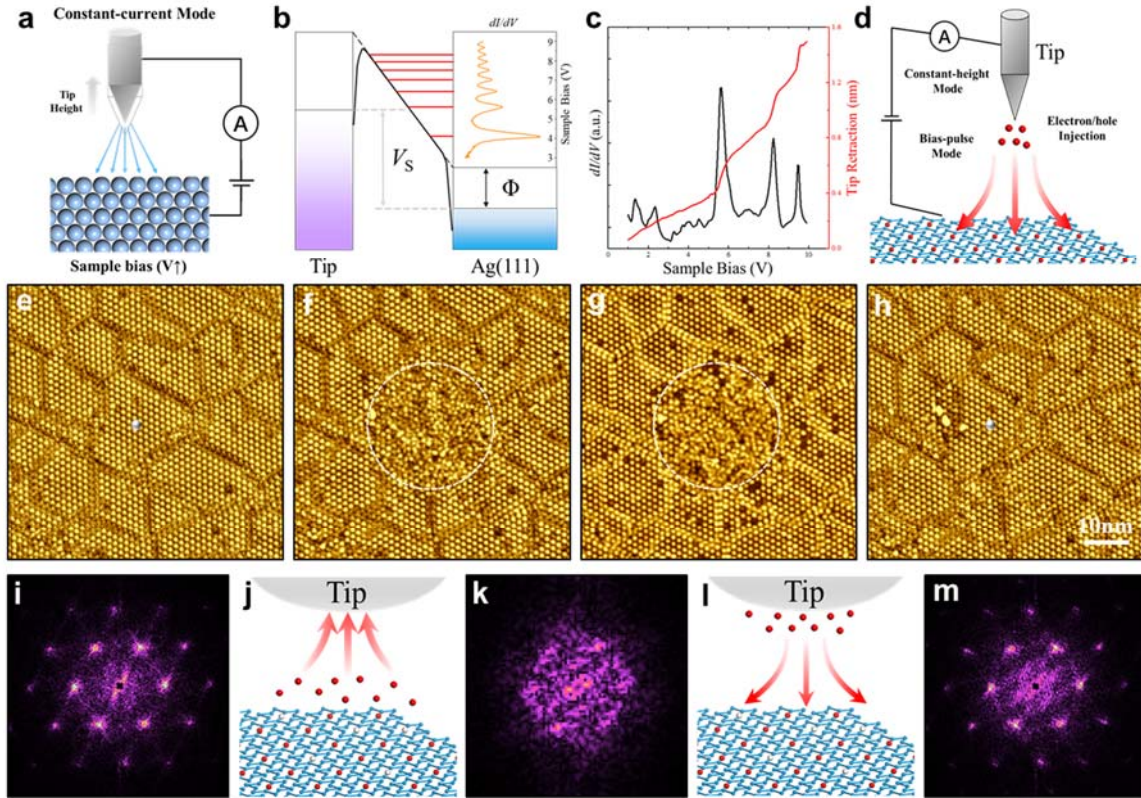


Figure 6. Local reversible manipulation of correlated CDW state by field-emission-induced charge injection in 1T-TaS₂. (a) Schematic for the STM-based field emission resonance (FER) spectra measurement. (b) FER mechanism and spectra of Ag(111) surface. (c) FER spectra of the correlated CDW state. (d) Cartoon illustration for the field-emission-induced transient electron- and hole-injection. (e-h) STM images of correlated CDW state before (e) and after (f, g) transient hole-injection, and the recovered order CDW state (h) by transient electron-injection. (i-m) The corresponding FFT patterns (i, k, m) and transient charge-injection cartoons (j, l) during the reversible manipulation. Scanning parameter: (e, f, h) $V = -0.5\text{V}$, $I = -100\text{pA}$; (g) $V = 0.5\text{V}$, $I = 100\text{pA}$.

Local reversible CDW manipulation

The above titration-like investigations have been focused on the structural evolutions of correlated CDW state in 1T-TaS₂ by sequential structural hole-doping at the thermodynamically stable state. The real-space local titration-like investigations of the correlated CDW state are further performed by the transient non-equilibrium hole-/electron-doping through the field-emission charge injection of STM tip (Fig. 6 and Supplementary Fig. 13) [53-57]. The work functions of sample can be determined by the STM-based field emission resonance (FER) spectra, as schematically illustrated in Fig. 6a and 6b, and the representative FER spectra of Ag(111) is supplied with the measurement mechanism. The measured FER spectra of 1T-TaS₂ shown in Fig 6c determine a work

function of ~ 5.5 eV [58]. The local and controllable hole-injection and electron-injection can be realized by the site-specific field emission bias-pulse in the constant-height mode, as schematic shown in Fig. 6d.

The transient hole-injection was performed by field-emission STM bias-pulse (-6V) at a mosaic-like CDW state of Fig. 6e, which induce a local circular disordered CDW region, as shown in Fig. 6f and 6g. The transient electron-injection by the following field-emission STM bias-pulse (+6V) can reorder this disordered CDW region (Fig. 6h). It is noted that the transient hole-doping-induced disordered CDW state is an amorphous metastable quantum jamming state of strongly correlated electrons [29]. The corresponding FFT and charge-injection manipulation cartoons are shown in Fig. 6i-m, which is further illustrated by the transient band-filling-dependent electron-electron/electron-lattice interactions in the correlated CDW state (Supplementary Fig. 14) [59].

In summary, we have performed a comprehensive titration-like investigation on the correlated CDW state of 1T-TaS₂. By sequential structural hole-doping, the electron voids, phase domains, stacking disordering and mixed phase/chiral domains emergent within the correlated CDW states in a step-by-step way, consistent with the gradually reduced intralayer and interlayer electron-electron/electron-lattice correlations. The emergent intermediate ring-SoD clusters and nematic CDW states are also discovered and discussed based on the intralayer and interlayer chiral-overlapping interactions. The local reversible manipulation of correlated CDW state was demonstrated by the non-equilibrium charge-injection of STM field-emission spectra. Our work provides a promising way to further realize exotic quantum states via the delicate tuning of interior interactions in correlated electronic states.

Acknowledgments

This project was supported by the National Key R&D Program of China (MOST) (Grant No. 2023YFA1406500), the National Natural Science Foundation of China (NSFC) (No. 21622304, 61674045, 11604063, 11974422, 12104504), the Strategic Priority Research Program (Chinese Academy of Sciences, CAS) (No. XDB30000000), and the Fundamental Research Funds for the Central Universities and the Research Funds of Renmin University of China (No. 21XNLG27). Y.Y. Geng was supported by the Outstanding Innovative Talents Cultivation Funded Programs 2023 of Renmin University of China.

Author contributions

W.J., H.G., W.Z. and Z.C. conceived the research project. H.D., Y.G., L.L. and Z.C. performed the STM experiments and analysis of STM data. J.G., M.W., Y.L., L.H., F.P. and R.X. helped in the experiments. H.D., Y.G., W.Z. and Z.C. wrote the manuscript with inputs from all authors.

Competing Interests

The authors declare no competing financial interests.

Data Availability

The authors declare that the data supporting the findings of this study are available within the article and its Supplementary Information.

Materials and Methods

Single crystal growth of Ti-doped $1T$ -TaS₂.

The high-quality $1T$ -Ta_{1-x}Ti_xS₂ single-crystals were grown by chemical vapor transport (CVT) method. Ta (99.99%, Aladdin), TaCl₅ (99.99%, Aladdin), S (99.99%, Aladdin), and Ti (99.99%, Aladdin) powders with a nominal molar ratio of 1:0.02:2.05:x ($x = 0.3\%$, 0.8% , 2.5% , 4.2% , 6.3%) were mixed thoroughly and then loaded into quartz tubes (inner diameter/outer diameter/length: 14/16/200 mm). 0.15 g iodine ($\sim 5 \text{ mg/cm}^3$) was added into the quartz tube as transport agent. The quartz tubes were sealed under high vacuum of 1.33×10^{-3} Pa and then heated in a two-zone furnace for 7 days, where the temperatures of source and growth zones were kept at $960 \text{ }^\circ\text{C}$ and $860 \text{ }^\circ\text{C}$ respectively. The quartz tubes were removed quickly from the furnace and quenched into ice water to obtain the $1T$ phase. Large $1T$ -Ta_{1-x}Ti_xS₂ crystals with size up to 10 mm were collected for further characterization and measurement. X-ray diffraction (XRD), scanning electron microscopy (SEM), X-ray energy dispersive spectroscopy (EDS) were employed to determine the crystal structure, morphology, and composition of as-prepared samples. The Ti-doping contents of all samples agree with their nominal molar ratio of source materials, demonstrating the controllable synthesis.

Scanning tunneling microscopy (STM).

High-quality Ti-doped $1T$ -TaS₂ crystals were cleaved at room temperature in ultrahigh vacuum at a base pressure of 2×10^{-10} Torr, and directly transferred to the cryogen-free variable-temperature STM system (PanScan Freedom, RHK). Chemically etched W tips were used for STM measurement in constant-current mode. The STM tips were calibrated on a clean Ag(111) surface. Gwyddion was used for STM data analysis. The attempt to utilize scanning tunneling spectroscopy (STS) on the intermediate ring-SoD clusters and nematic CDW state has not obtained clear definitive results due to the thermal broadening effect and the inherent instability of the STM junction at $\sim 50\text{K}$.

References:

1. Thorne R. E. Charge-density-wave conductors. *Physics Today* **49** (5), 42-47 (1996).
2. Wilson J. A., *et al.* Charge-density waves and superlattices in the metallic layered transition metal dichalcogenides. *Advances in Physics* **24:2**, 117-201 (1975).
3. Han G.H., *et al.* Van der Waals metallic transition metal dichalcogenides. *Chem. Rev.* **118** (13):6297-6336 (2018).
4. Manzeli S., *et al.* 2D transition metal dichalcogenides. *Nat. Rev. Mater.* **2** (8):17033 (2017).
5. Tan C.L., *et al.* Recent advances in ultrathin two-dimensional nanomaterials. *Chem. Rev.* **117** (9):6225-6331 (2017).
6. Bao C. H., Distinguishing and controlling Mottness in 1T-TaS₂ by ultrafast light. *Phys. Rev. B* **107**, L121103 (2023).
7. Ohta S., *et al.* Electronic state modulation of the Star of David lattice by stacking of $\sqrt{13} \times \sqrt{13}$ domains in 1T-TaSe₂. *Phys. Rev. B* **104**, 155433 (2021).
8. Wang Z.L., *et al.* Flat band in hole-doped transition metal dichalcogenide observed by angle-resolved photoemission spectroscopy. *Chin. Phys. B* **32**, 067103 (2023).
9. Nakata Y., *et al.* Robust charge-density wave strengthened by electron correlations in monolayer 1T-TaSe₂ and 1T-NbSe₂. *Nat. Commun.* **12**, 5873 (2021).
10. Lee S., Origin of the insulating phase and first-order metal-insulator transition in 1T-TaS₂. *Phys. Rev. Lett.* **122**, 106404 (2019).
11. Wilson, J.A., *et al.* Charge-density waves in metallic, layered, transition-metal dichalcogenides. *Phys. Rev. Lett.* **32**, 882-885 (1974).
12. Geng Y.Y., *et al.* Hysteretic electronic phase transitions in correlated charge-density-wave state of 1T-TaS₂. *Phys. Rev. B* **107** 195401 (2023).
13. Kranjec A., *et al.* Electronic dislocation dynamics in metastable Wigner crystal states. *Symmetry* **14**, 926 (2022).
14. Mraz A., *et al.* Manipulation of fractionalized charge in the metastable topologically entangled state of a doped Wigner crystal. *Nat. Commun.* **14**, 8214 (2023).
15. Rossnagel, K. & Smith, N.V., Spin-orbit coupling in the band structure of reconstructed 1T-TaS₂. *Phys. Rev. B* **73**, 073106 (2006).
16. Law, K.T. & Lee, P.A., 1T-TaS₂ as a quantum spin liquid. *Proc. Natl. Acad. Sci.* **114**, 6996-7000 (2017).
17. Klanjšek, *et al.* A high-temperature quantum spin liquid with polaron spins. *Nat. Phys.* **13**, 1130-1134 (2017).
18. Ruan W., *et al.* Evidence for quantum spin liquid behaviour in single-layer 1T-TaSe₂ from scanning tunneling microscopy. *Nat. Phys.* **17**, 1154-1161 (2021).
19. Nayak A. K., *et al.* Evidence of topological boundary modes with topological nodal-point superconductivity. *Nat. Phys.* **17**, 1413-1419 (2021).
20. Ribak A., *et al.* Chiral superconductivity in the alternate stacking compound 4Hb-TaS₂. *Sci. Adv.* **6**, eaax9480 (2020).
21. Cho D., *et al.* Nanoscale manipulation of the Mott insulating state coupled to charge order in 1T-TaS₂. *Nat. Commun.* **7**, 10453 (2016).
22. Cho D., *et al.* Correlated electronic states at domain walls of a Mott-charge-density-wave insulator 1T-TaS₂. *Nat. Commun.* **8**, 392 (2017).
23. Ma L., *et al.* A metallic mosaic phase and the origin of Mott-insulating state in 1T-TaS₂. *Nat. Commun.* **7**, 10956 (2016).

24. Li Y., *et al.* Electronic states of domain walls in commensurate charge density wave ground state and mosaic phase in $1T$ -TaS₂. *Chin. Phys. B* **32**, 077101 (2023).
25. Mihailovic D., The importance of topological defects in photoexcited phase transitions including memory applications. *Appl. Sci.* **9**, 890 (2019).
26. Park J.W., *et al.* Zoology of domain walls in quasi-2D correlated charge density wave of $1T$ -TaS₂. *NPJ Quantum Mater.* **6**, 32 (2021).
27. Skolimowski J., *et al.* Mottness collapse without metallization in the domain wall of the triangular-lattice Mott insulator $1T$ -TaS₂. *Phys. Rev. Lett.* **122**, 036802 (2019).
28. Karpov P., *et al.* Modeling of networks and globules of charged domain walls observed in pump and pulse induced states. *Sci. Rep.* **8**, 4043 (2018).
29. Gerasimenko Y.A., *et al.* Quantum jamming transition to a correlated electron glass in $1T$ -TaS₂. *Nat. Mater.* **18** 1078-1083 (2019).
30. Sipoş B., *et al.* From Mott state to superconductivity in $1T$ -TaS₂. *Nat. Mater.* **7**, 960-965 (2008).
31. Shen S. W., *et al.* Inducing and tuning Kondo screening in a narrow-electronic-band system. *Nat. Commun.* **13**, 2156 (2022).
32. Dong H.Y., *et al.* Emergent electron-based Kagome lattice in correlated charge-density-wave state of $1T$ -TaS₂. *arXiv*: 2301.05885 (2023).
33. Lee D., *et al.* Tunable Mott Dirac and Kagome bands engineered on $1T$ -TaS₂. *Nano. Lett.* **22**, 7902-7909 (2022).
34. Yu Y. J., *et al.* Gate-tunable phase transitions in thin flakes of $1T$ -TaS₂. *Nat. nanotech.* **10**, 270-276 (2015).
35. Gerasimenko Y.A., *et al.* Intertwined chiral charge orders and topological stabilization of the light-induced state of a prototypical transition metal dichalcogenide. *NPJ Quantum Mater.* **4**, 32 (2019).
36. Zhang J., *et al.* Photoexcitation induced quantum dynamics of charge density wave and emergence of a collective mode in $1T$ -TaS₂. *Nano Lett.* **19** 6027-6034 (2019).
37. Lee J., *et al.* Distinguishing a Mott insulator from a trivial insulator with atomic adsorbates. *Phys. Rev. Lett.* **126**, 196405 (2021)
38. Lee D., *et al.* Tunable Mott Dirac and Kagome bands engineered on $1T$ -TaS₂. *Nano. Lett.* **22**, 7902-7909 (2022).
39. Lee J., *et al.* Honeycomb-Lattice Mott Insulator on Tantalum Disulphide. *Phys. Rev. Lett.* **125**, 096403 (2020).
40. Jarc G., *et al.* Cavity-mediated thermal control of metal-to-insulator transition in $1T$ -TaS₂. *Nature* **622** 487 (2023).
41. Ritschel T., *et al.* Stacking-driven gap formation in layered $1T$ -TaS₂. *Phys. Rev. B* **98**, 195134 (2018).
42. Gao J.J., *et al.* Chiral charge density waves induced by Ti-doping in $1T$ -TaS₂. *Appl. Phys. Lett.* **118**, 213105 (2021).
43. Bediako D.K., *et al.* Encoding multistate charge order and chirality in endotaxial heterostructures. *Nat. Commun.* **14**, 6031 (2023).
44. Song X., *et al.* Atomic-scale visualization of chiral charge density wave superlattices and their reversible switching. *Nat. Commun.* **13**, 1843 (2022).
45. Xi X.X., *et al.* Electronical switching of ferro-rotational order in nanometer-thick $1T$ -TaS₂ crystals. *Nat. Nanotech.* **18** 854-860 (2023).
46. Cho D., *et al.* Charge density wave surface reconstruction in a Van der Waals layered material. *Nat. Commun.* **14**, 5735 (2023).
47. Butler C.J., *et al.* Mottness versus unit-cell doubling as the driver of the insulating state in $1T$ -TaS₂. *Nat.*

Commun. **11**, 2477 (2020).

48. Butler C.J., *et al.* Doublonlike excitations and their phononic coupling in a Mott charge-density-wave system. *Phys. Rev. X* **11**, 011059 (2021).
49. Zou X.L., *et al.* Probing complex stacking in a layered material via electron-nuclear quadrupolar coupling. *Phys. Rev. Lett.* **7**, L091001 (2023).
50. Pizarro J.M., *et al.* Deconfinement of Mott localized electrons into topological and spin-orbit-coupled Dirac fermions. *NPJ Quantum Mater.* **5**, 79 (2020).
51. Yao Q., *et al.* Engineering domain wall electronic states in strongly correlated van der Waals material of 1T-TaS₂. *Nano Lett.* **21**, 9699-9705 (2021).
52. Naik G.V., *et al.* Reorganization of CDW stacking in 1T-TaS₂ by an in-plane electrical bias. *APL Mater.* **9** 111103 (2021).
53. Zhang Q., *et al.* Bandgap renormalization and work function tuning in MoSe₂/hBN/Ru(0001) heterostructures. *Nat. Commun.* **7**, 13843 (2016).
54. Craes F., *et al.* Mapping image potential states on Graphene quantum dots. *Phys. Rev. Lett.* **111**, 056804 (2013).
55. Liu S., *et al.* Plasmon-assisted resonant electron tunneling in a scanning tunneling microscope junction. *Phys. Rev. Lett.* **121**, 226802 (2018).
56. Werner W.S.M., *et al.* Scanning tunneling microscopy in the field-emission regime: Formation of a two-dimensional electron cascade. *Appl. Phys. Lett.* **115**, 251604 (2019).
57. Schulz F., *et al.* Epitaxial hexagonal boron nitride on Ir(111): A work function template. *Phys. Rev. B* **89**, 235429 (2014).
58. Toshihiro S., *et al.* Work function and photothreshold of layered metal dichalcogenides. *Jpn. J. Appl. Phys.* **33** 2696 (1994)
59. Shao D. F., *et al.* Manipulating charge density waves in 1T-TaS₂ by charge-carrier doping: A first-principles investigation. *Phys. Rev. B* **94**, 125126 (2016).